Insight into CO induced degradation mode of Pd/SSZ-13 in NOx adsorption and release: Experiment and modeling

Chemical Engineering Journal 439 (2022) 135714

Contents lists available at ScienceDirect

Chemical Engineering Journal

journal homepage: www.elsevier.com/locate/cej

Insight into CO induced degradation mode of Pd/SSZ-13 in NO_x adsorption and release: Experiment and modeling

Dawei Yao [a], Rojin Feizie Ilmasani [a], Johann C. Wurzenberger [b], Thomas Glatz [b], Joonsoo Han [a], Phuoc Hoang Ho [a], Derek Creaser [a], Louise Olsson [a,*]

[a] Chemical Engineering division, Competence Center for Catalysis, Chalmers University of Technology, Göteborg SE-41296, Sweden
[b] AVL List GmbH, Graz, Austria

ARTICLE INFO

Keywords:
Passive NO_x adsorber (PNA)
Kinetic model
Pd sintering
Ostwald ripening
Particle migration

ABSTRACT

Passive NO_x adsorption (PNA) on Pd zeolites is an important technique to remove NO_x during the cold start of the engine. However, the stability of Pd zeolites under high concentrations of CO is still challenging in multiple cold starts of an engine. Herein, we illustrate the CO-induced degradation mechanism of Pd zeolite by combining experiments and kinetic models. Pd/SSZ-13 has been used in multicycle processes containing NO_x adsorption at low temperature and temperature programmed desorption, which represents the PNA degradation in multiple cold start periods. A kinetic model was developed to describe the NO_x storage and degradation behavior of Pd/SSZ-13. Both experimental and modelling observations suggested that two Pd sintering modes are occurring under high CO concentration (4000 ppm), namely Ostwald ripening and particle migration. Apart from the degradation behavior, this model is also adequate for describing multi-cycle NO_x storage and release behavior under low CO concentration.

1. Introduction

With the increase of automotive market, the concerns for nitrogen oxides (NO_x) generation substantially grows in many countries [1]. The application of technologies such as lean NO_x traps (LNT) [2,3] and NH_3 selective catalytic reduction (SCR) [4,5] and can significantly reduce vehicle NO_x emissions. However, owing to the kinetic limitations of the LNT and that urea cannot be dosed at low temperature for the SCR system (around 200 °C is typically needed), these systems cannot effectively reduce NO_x emissions in cold start periods of the engine [6]. Accordingly, to further reduce the NO_x emission, passive NO_x adsorber (PNA) module has recently been applied in front of the SCR device in the aftertreatment system. During the cold start, the NO_x is adsorbed by PNA at low temperatures. After the engine warms up, the adsorbed NO_x releases at a higher temperature (≥200 °C). The high temperature assists the urea dosing in the following SCR system [7], subsequently converting NO_x to N_2 and H_2O.

Pd zeolites are widely used for PNA owing to their resistance towards H_2O and SO_2 [6], and they also have shown a high NO_x desorption temperature [8,9]. The NO_x adsorption on Pd zeolites have been examined under realistic gas conditions, including NO_x, O_2, H_2O and CO. Although the roles of O_2 and H_2O are widely accepted for the regeneration of the PNA [10] and suppressing the NO_x adsorption on Pd sites [11,12], the influence of CO is still questionable. It has been found that CO influences the Pd zeolite in distinctive manners under different conditions. Under low CO concentration (100 ~ 600 ppm), CO contributes to stabilize NO_x species by reducing the Pd(II) to lower valence, resulting in an increased amount of adsorbed NO_x and a higher temperature for desorption [9,11,13,14]. Kinetic models were further developed, based on these mechanisms to predict the NO_x adsorption behavior under low CO concentration [15,16], as well as in presence of hydrocarbons [15].

However, the CO concentration in the cold-start can be much higher, e.g. Fang et al [17]. observed about 3500 ppm CO during the cold start of a diesel engine, which increased to 4000 ppm when the engine run at an altitude of 1000 m. A high CO concentration is problematic, because it results in a substantial degradation of the Pd zeolite occurs during multi-cycle NO_x adsorption [8,18,19]. It has been found that CO induced Pd sintering is the main reason for degradation [19], but the precise sintering mechanisms have not yet been reported.

There is according to our knowledge, no kinetic models available that can describe the CO-induced Pd zeolite degradation in multi-cycle

* Corresponding author.
E-mail address: louise.olsson@chalmers.se (L. Olsson).

https://doi.org/10.1016/j.cej.2022.135714
Received 3 December 2021; Received in revised form 10 February 2022; Accepted 8 March 2022
Available online 9 March 2022

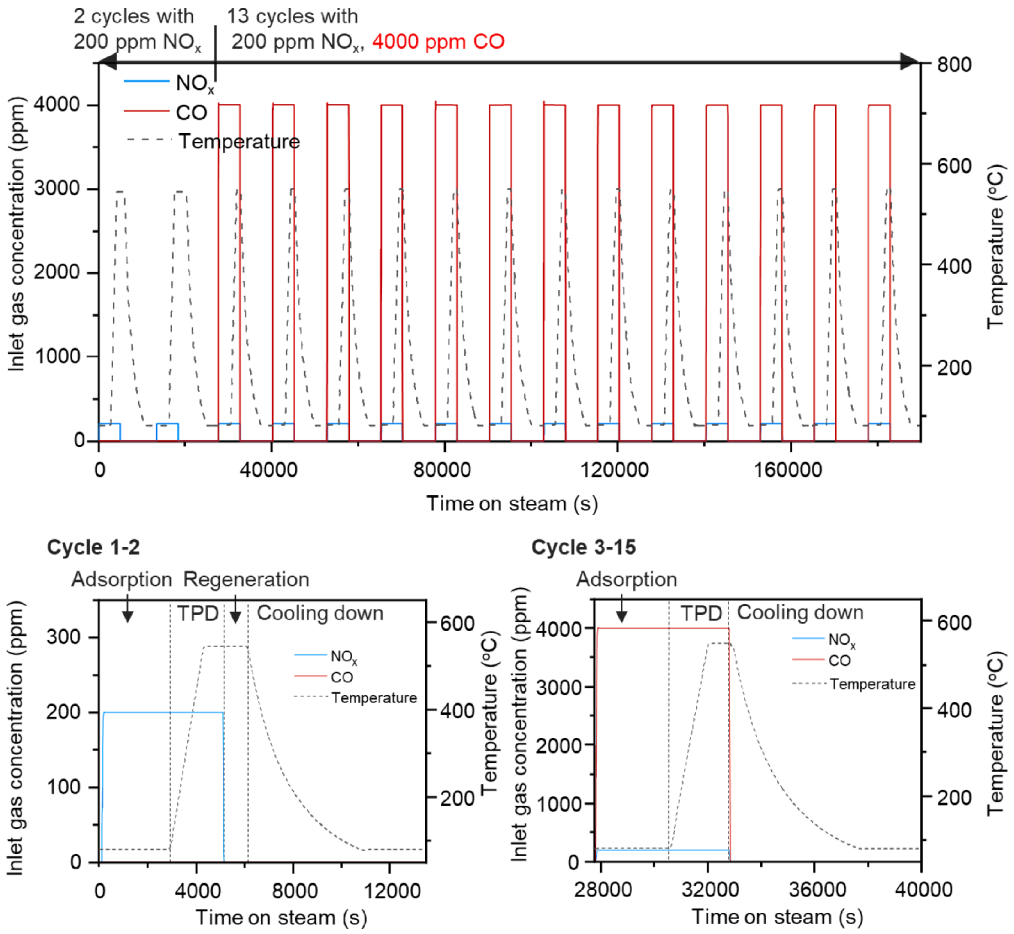

Fig. 1. Evaluation procedure of multi-cycle PNA test under 0 ppm CO (cycles 1–2) and 4000 ppm CO (cycles 3–15). Other inlet gas conditions: 200 ppm NO_x (196 ppm NO and 4 ppm NO_2), 8%O_2, 5%H_2O, balanced in Ar.

NO_x adsorption, which is the objective of the current study. Owing to the very different influences of CO under varied concentrations on Pd zeolite, there is no kinetic model established so far that could be applied for describing both the CO-assisted NO_x storage and CO-induced Pd zeolite deactivation. Herein, we established a kinetic model with 37 reactions that could describe the degradation of Pd zeolite in multi-cycle NO_x adsorption and desorption tests under high CO concentration. This kinetic model could also be successfully applied in describing NO_x behavior under low CO concentration. Pd/SSZ-13 was used for this kinetic study because the small-pore zeolites with palladium have been shown to exhibit a high NO_x desorption temperature [20]. The Pd/SSZ-13 was used in multicycle NO_x adsorption and desorption process, with different composition of inlet gases (200 ppm NO_x, 0–200-400–4000 ppm CO, 8%O_2, 5%H_2O). The Pd/SSZ-13 degradation was first investigated using several characterization techniques in order to develop the reaction mechanism. The model is established based on our previous model containing three Pd sites ($Z^-[Pd(II)OH]^+$, $Z^-Pd(II)Z^-$ and PdO) initially and 18 reactions [16]. By combining experiments and kinetic models, we found that the Pd/SSZ-13 degradation is induced by Pd sintering under high CO concentration, which contains Ostwald ripening and particle migration sintering modes. This model well describes the multi-cycle NO_x storage and release behavior under both low CO concentration and high CO concentration. Furthermore, both the CO-assisted NO_x storage and CO-induced Pd/SSZ-13 degradation could be illustrated from the kinetic model.

2. Experimental methods

2.1. Materials and chemicals

NaOH (ACS reagent, ≥97.0%, pellets), $Al(OH)_3$ (reagent grade), fumed silica (7 nm average particle size), and Palladium(II) nitrate solution (10 wt% in 10 wt% nitric acid, 99.999%) were purchased from Sigma-Aldrich. N,N,N,-Trimethyl-1-adamantylammonium hydroxide (TMAda-OH, 25% in water) was purchased from TCI.

2.2. Catalysts synthesis

According to the previously reported hydrothermal method [21], SSZ-13 with a ratio of Si/Al = 12 was synthesized. Firstly 0.8 g NaOH was dissolved in 66 g deionized water, followed by the addition of 17.68 g TMAda-OH with stirring. Subsequently, 1.38 g of Aluminum hydroxide and 12 g of SiO_2 (~100 nm of diameter) were added to the mixture, and stirring vigorously stirred until the mixture was homogeneous as gel. The mixture was poured in two autoclaves (75-mL Teflon lining with stainless-steel shell). The autoclaves were placed inside two sand baths, which were placed on heating plates. Then the autoclaves were heated to 160 °C and kept for 96 h with constant stirring. After cooling down, the samples were collected and washed with deionized water three times. The obtained samples were dried at 120 °C for 12 h to obtain white powder, followed by a calcination at 600 °C in air for 8 h to produce Na-SSZ-13. To transform Na-SSZ-13 to H-SSZ-13 via ion exchange process, the powder was added into 143.23 g NH_4NO_3 solution (30.2 wt%), then kept under 80 °C for 2 h with stirring. The obtained sample was further washed by deionized water and separated by

centrifugation. This ion exchange process was repeated twice. Finally, the sample was dried at 120 °C for 12 h and thereafter calcined at 600 °C for 8 h to remove NH_4^+ and produce H-type SSZ-13.

An incipient wetness impregnation method was used to load 1 wt% Pd (derived from $Pd(NO_3)_2$) into SSZ-13. The obtained sample was dried overnight at 100 °C, and then calcined in air at 500 °C for 5 h.

2.3. Monolith preparation

The obtained Pd/SSZ-13 samples were firstly loaded on monoliths for PNA evaluation. The monolith was made by cordierite with a honeycomb structure (400 cpsi) with the size of 2 cm (length) × of 2.1 cm (diameter). After cutting, a calcination procedure was conducted 550 °C for 2 h. Boehmite (Dispersal P2) was added as an inactive binder in to Pd/SSZ-13 with a weight ratio of 5:95, and dissolved in 1:1 EtOH/H_2O solution (volume ratio). The obtained slurry was dropped over all the channels of the monolith until it passed through all the channels completely. After dropping, a stream of hot air at 90 °C was used to remove excess slurry. The slurry dropping and removing process on the monolith was conducted multiple times to load 700 mg washcoat. After coating, the monolith was calcined for 5 h at 500 °C.

2.4. Reactor system

The flow reactor system for NO_x adsorption and desorption has been described in our previous studies [16,22]. The monolith was put into a quartz tube, with two thermocouples placed inside the monolith and directly in front of the monolith. The feed gases are adjusted by several mass flow controllers (from Bronkhorst). Another controlling system evaporated H_2O and mixed with Ar to the reactor. A FTIR spectrometer (MKS Multigas 2030) was placed at the outlet of the reactor to detect the concentration of the outlet gases.

2.5. Degreening of the monoliths

To generate more ion-exchanged Pd sites and stabilize the Pd sites, the monoliths were firstly degreened in a flow reactor before evaluation and characterization [23]. The monolith was first placed into the reactor system. Then the temperature was increased to 750 °C with a rate of 20 °C/min and kept for 1 h, with an inlet gas flow of 400 ppm NO_x, 8% O_2 and 5% H_2O diluted in Ar. The total flow rate of inlet gases was 750 mL/min. Then the reactor was cooled down to room temperature for further evaluation procedures or characterization.

2.6. Catalyst evaluation

The degreened sample was tested in the same reactor system. To simulate the multiple cold start periods, the experimental procedure includes multicycle NO_x adsorption, temperature program desorption (TPD) and pretreatment. The first 2 cycles were conducted without adding CO, while cycles 3–15 were conducted in the presence of 4000 ppm CO to investigate the degradation. The detailed temperature and inlet gas program are shown in Fig. 1.

2.7. Characterization

All catalyst characterization experiments were conducted on scraped of wash-coat after degreening or multi-cycle experiments, except for ICP-SFMS.

Inductively coupled plasma sector field mass spectrometry (ICP-SFMS) was used to analyze the Si, Al and Pd content of the catalyst. This characterization was performed by ALS Scandinavia AB.

X-ray diffraction (XRD) was performed by using a SIEMENS diffractometer D5000 at 40 kV and 40 mA using Cu Kα radiation (λ = 1.5418 Å) filtered at room temperature. Scanning was conducted from 5° to 50° at a rate of 1°/min.

Transmission electron microscope (TEM) images were obtained via a FEI Tecnai with an operating voltage of 200 kV. Scanning transmission electron microscopy (STEM) images were obtained at various magnifications using a FEI Titan 80–300 with a high angle annular dark field detector (HAADF), with an operating voltage of 300 kV. The degreened sample powder was firstly mixed in EtOH with ultrasound. Then the solid–liquid mixture was dropped onto a porous carbon film supported by a copper grid (3 mm). The elemental mapping of Pd, Si, Al was further conducted by the equipped energy dispersive X-ray (EDX, Oxford Inca).

CO irreversible adsorption was performed by Micromeritics ASAP 2020 Chemi Plus with a chemisorption module. The sample was first treated under vacuum at 200 °C for 1 h to remove any contaminates, then cooled to 35 °C under vacuum. A total adsorption isotherm was collected from 130 to 800 mbar CO. After the first CO adsorption cycle the sample was evacuated for 30 min to remove the physiosorbed CO, and the measurement was repeated to determine the reversible adsorption isotherm. The irreversible isotherm adsorption is obtained from the asymptotic value of the total adsorption isotherm in the first cycle adsorption and the reversible adsorption isotherm is obtained from the second cycle adsorption.

H_2 temperature programmed reduction (H_2-TPR) was conducted for the Pd/SSZ-13 samples after PNA evaluation. The evaluated monoliths were crushed into pellets and 50 mg was loaded into a quartz tube featuring a gas and temperature controlling system. The total flow rate of the inlet gases was set to 20 mL/min. The sample was firstly treated with 7% O_2/Ar at 500 °C for 1 h. After cooling down to 25 °C, 0.2% H_2/Ar was added, and the temperature was ramped up to 600 °C with a rate of 10 °C/min. A mass spectrometer (Hiden HPR-20 QUI) was used to detect the outlet gases.

The in-situ diffuse reflectance infrared Fourier transform spectroscopy (DRIFTS) of the adsorption of NO and CO on Pd/SSZ-13 was investigated via A Bruker Vertex 70 spectrometer. An MCT detector with a scanning resolution of 4 cm^{-1} was used as spectrometer. A sealed chamber with KBr windows for diffuse reflection was used for placing the sample (~20 mg).

3. Kinetic modeling

3.1. Reactor model

The kinetic model was simulated by the Aftertreatment Module installed in the software AVL BOOST^{TM} (2020 R2) through a single-channel model. The specific heat capacity and thermal conductivity properties of the material are referred to Property Database of Cordierite Materials in AVL CRUISE^{TM} M.

For developing the kinetic model, 20 grid points are set for the discretization along the monolith channel. The mass transfer inside the washcoat is set to 5 grid points. The mass balance equations are described in detail in our earlier work [16].

The external mass transfer from the bulk gas to the washcoat surface is simulated according to the film model, as defined by Eq. (1) [24].

$$GSA \times k_{k,m} \times (y_k - y_k^B) = \sum_i^{nr} v_{i,k} \times r_i(y_k, T_s, \theta_k) \quad (1)$$

where $k_{k,m}$ is the mass transfer coefficient (mol/(m^2 s)), GSA is geometric surface area per reactor volume (m^{-1}) (see [16]), $v_{i,k}$ and r_i are the stoichiometric coefficient for specie k and reaction rate for reaction i (mol/(m^2 s)). y_k and $y^B{}_k$ are the mole fractions for specie k in the reaction layer and the bulk, respectively. T_s is the temperature in the solid phase (K). According to Chatterjee et al. [25], the internal mass transfer was considered as a constant pore diffusion model, where the effective diffusion rates of components are $5 \times 10^{-6} m^2/s$. This method has also been used in several of our previous aftertreatment-system models [26–31].

The solid phase energy balance equation is given by Eq. (2).

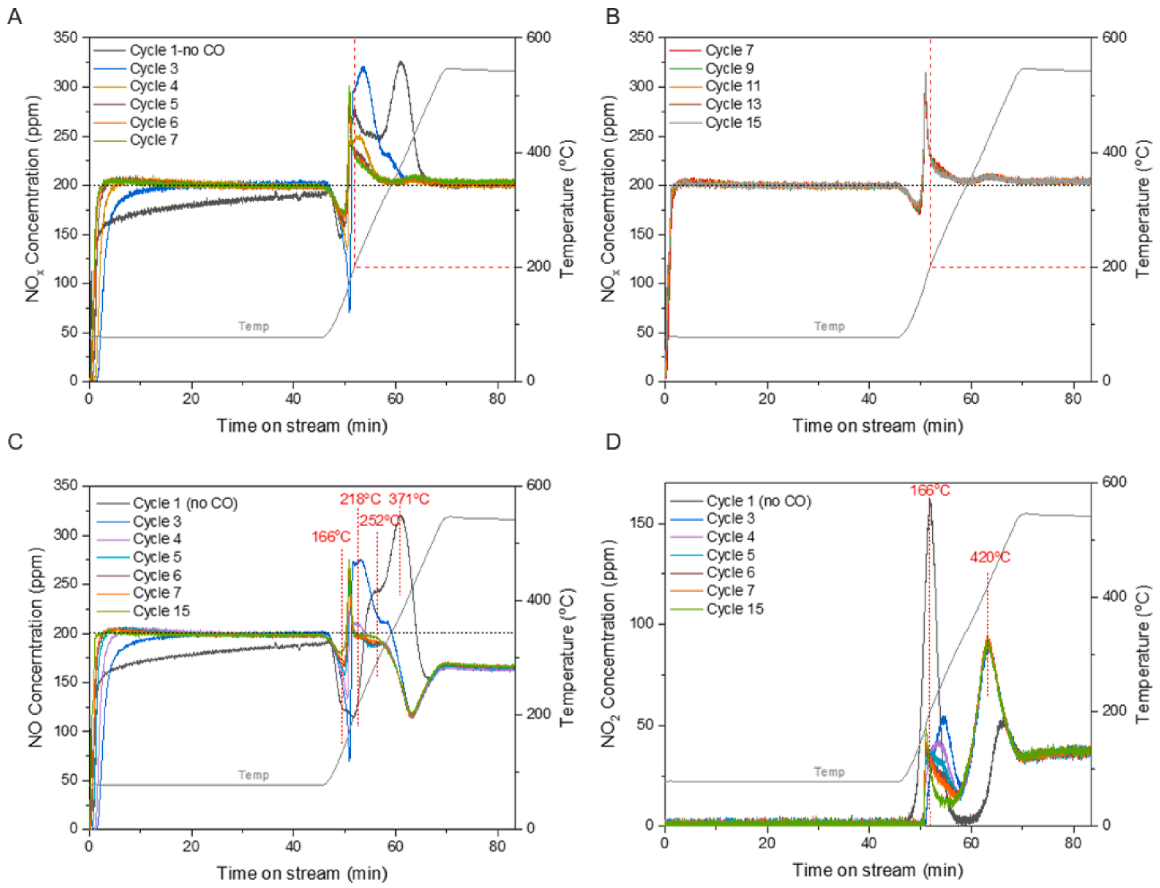

Fig. 2. Multi-cycle NO_x adsorption and TPD test in selected cycles. A, B: NO_x profiles in cycle 1–7 and cycle 7–15, NO (C) & NO_2 (D) during NO_x adsorption and TPD. Reaction conditions are shown in Fig. 1.

$$\left(1-\varepsilon_g\right)\times\rho_s\times\frac{\partial\left(c_{p,s}\times T_s\right)}{\partial t}=\left(1-\varepsilon_g\right)\times\frac{\partial}{\partial z}\left(\lambda_s\frac{\partial T_s}{\partial z}\right)-GSA\times k_h\times\left(T_s-T_g\right)+\sum_i^I\Delta h_i\times r_i\left(c_k^L,T_s\right)+q_{ext}\quad(2)$$

where ε_g is volume fraction of gas phase in the total system, ρ_s is the density of the solid phase (kmol/m^3), λ_s is its thermal conductivity (W/(m·K)), k_h is the heat transfer coefficient between the solid walls and the gas phase (W/(m^{2}K)), T_g is the temperature in the gas phase (K), Δh is the heat of reaction of the catalytic surface reactions and the surrounding heating is captured with q_{ext}. The overall heat flux was given by Eq. (3):.

$$\frac{q_{ext}}{\Delta z}=k_{out}\times d_{mon}\times\pi\times\left(\mathrm{T}_s(\mathrm{z},\mathrm{r}=\mathrm{R})-\mathrm{T}_{hea}\right)\quad(3)$$

where k_{out} is overall heat transfer coefficient (W/(m^{2}K)), d_{mon} is monolith diameter (m), T_{hea} is heating temperature (K). Owing to the low heat of reaction in the process of NO_x adsorption and desorption, and the low concentration of NO_x, the reaction heat for NO adsorption and oxidation can be neglected in the kinetic model. This method has been applied in several kinetic models containing NO_x adsorption [26,28,30,32,33]. The concentration of CO was 4000 ppm in the PNA process, thus the reaction heat of CO oxidation was significant and modeled according to the thermal database of AVL user coding interface. The monolith is very short and surrounded by a long heating coil. The inlet gas temperature for modeling was set according to the temperature detected in front of the monolith, and heating temperature was set according to the measured temperature in the center of the monolith.

3.2. Kinetic model

In our recent work [16] we examined the NO_x adsorption on Pd/SSZ-13 under low CO concentration and developed a kinetic model that described NO_x adsorption on Pd/SSZ-13 under 0–400 ppm CO, 200–400 ppm NO_x. The reactions mechanism of this model is listed as Reactions (1)–(18) (R1-R18) in Table S1, and the corresponding parameters are listed in Table S2. Three palladium sites were used initially, $Z^-[Pd(II)OH]^+$, $Z^-Pd(II)Z^-$ and PdO, in this model to describe the storage of NO_x. The $Z^-[Pd(II)OH]^+$ and PdO species were reduced by 200 ~ 400 ppm CO to produce $Z^-Pd(I)^+$, Z^-H^+-Pd(0) and Pd(0), which afforded a higher stability to store NO_x species and a release temperature above 200 °C, which is effective for urea dosing. This kinetic model can be used for describing NO_x adsorption and release under low CO concentration (200 ~ 400 ppm CO) in multicycle PNA tests [16]. The kinetic model in this work that describes degradation mechanism under high CO concentration is an expansion of the previous work. The objective of this model is to describe multicycle PNA behavior under a larger range of CO concentration (0 ~ 4000 ppm).

The AVL User Coding Interface embedded with ANSI C programming language was used for defining the reaction rate expression. The reaction rate is calculated according to the Arrhenius equation in Eq. (4):.

$$k_i=A_i e^{\frac{-E_{A,i}}{(RT_s)}}\quad(4)$$

where k_i is rate constant for reaction i (s^{-1}), A_i is pre-exponential factor for reaction i (s^{-1}), $E_{A,i}$ is activation energy for reaction i (J/mol). It has been generally reported that the NO_x adsorption is a non-activated process [10,34,35], indicating the activation energy for NO_x adsorption should be 0. A linear correlation between activation energy and

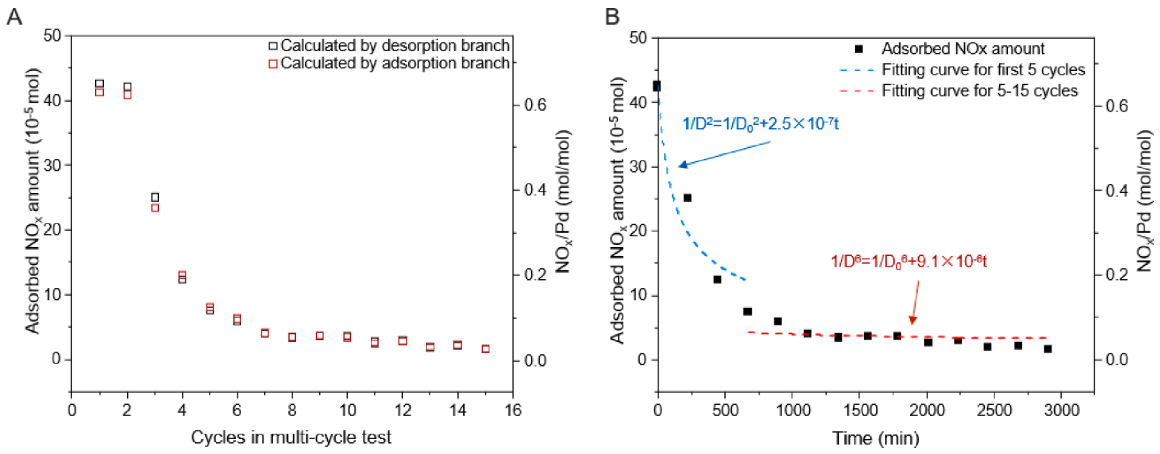

Fig. 3. Adsorbed NO_x amount and NO_x/Pd ratio in a multi-cycle PNA test as a function of cycles (A) and time (B) with fitting curve. The data was fitted according to the deactivation equation (1)/$D^n = 1/D_0^n + kt$. D and D_0 are the dispersion at time t and time 0, respectively, and n is the exponent in the power law, dependent on the deactivation stage [37,38].

adsorption coverage was used for NO/NO_2 desorption on Cu/ZSM-5 [34] and Pd/SSZ-13 [16]. We here use the same method in desorption activation energy determined by the Temkin isotherm, according to Eq. (5):.

$$E_{NO_x,des} = E^0_{NO_x,des}(1 - \alpha_i \theta_{NO_x}) \quad (5)$$

where $E^0_{A,i}$ is the activation energy at zero coverage for reaction i (J/mol), α_i is coverage dependence in reaction i.

4. Result and discussion

4.1. Physical and chemical properties of Pd/SSZ-13

Pd/SSZ-13 was applied in evaluating NO_x adsorption and TPD performance under high CO concentration (4000 ppm) with the existence of O_2 and H_2O. This particular Pd/SSZ-13 batch has also been characterized in our previous study, where a kinetic model was developed for PNA over Pd/SSZ-13 [16]. The Pd/SSZ-13 contains 0.98 wt% Pd with a Si/Al molar ratio of 12, as measured from ICP-SFMS. The pore volume of Pd/SSZ-13 is 0.30 cm^3/g and the specific surface area is 659 m^2/g. The washcoat thickness of another monolith sample (prepared using the same batch of Pd/SSZ-13 and the same preparation procedure) is 70 ± 40 μm as determined from SEM measurements [16].

4.2. Pd/SSZ-13 degradation under high CO concentration

In order to investigate the CO induced degradation of Pd/SSZ-13 during multiple cold start periods, the monolith was tested by multi-cycle NO_x adsorption and a TPD procedure under 200 ppm NO_x (196 ppm NO and 4 ppm NO_2), 0/4000 ppm CO, 8% O_2 and 5% H_2O. The detailed evaluation processes are shown in Fig. 1. The first 2 cycles were evaluated for Pd/SSZ-13 without CO adding for checking the initial NO_x storage behavior, then 4000 ppm CO was added from cycle 3 to cycle 15. The $NO_x/NO/NO_2$ profiles in selected cycles are shown in Fig. 2. All the profiles are aligned according to the time points of NO_x addition (set to 0). The NO_x profiles for cycle 1 and cycle 2 are compared in Figure S1, illustrating there is no deactivation on Pd/SSZ-13 in the absence of CO. We have used three initial Pd sites in Pd/SSZ-13, which are $Z^-Pd(II)Z^-$, $Z^-[Pd(II)OH]^+$ cation sites and PdO cluster on the SSZ-13 surface, in our previous kinetic model [16]. In NO_x adsorption and desorption process, $Z^-[Pd(II)OH]^+$ was reduced by NO and produced $Z^-Pd(I)^+$, which showed a stronger ability for storing NO_x. PdO reacted with NO and form $Pd(NO_3)_2$ species and subsequently decomposed to generate NO_2 at higher temperature. In cycle 1 of this work, the peaks of NO desorption at 252 °C and 371 °C are respectively attributed to NO desorption from $Z^-Pd(II)Z^-$ and $Z^-Pd(I)^+$. The NO consumption peak and NO_2 desorption peak at 166 °C are attributed to the $Z^-[Pd(II)OH]^+$ reduction, Pd $(NO_3)_2$ formation and decomposition.

After adding 4000 ppm CO in cycle 3, the NO_x desorption peaks were gradually decreased in the first 3–7 cycle, while those peaks in 7–15 cycles were quite similar. This result indicates that most of the degradation of Pd/SSZ-13 happened in the early cycles. The NO profiles in Fig. 2C show that the desorption peak of NO from $Z^-Pd(II)Z^-$ (252 °C) and $Z^-Pd(I)^+$ (371 °C) decreased and then disappeared, while another peak was appearing at 218 °C. The NO_2 desorption peak also decreased and shifted to lower temperatures with increased cycle number. It could be deduced from these results that the initial $Z^-Pd(II)Z^-$, $Z^-[Pd(II)OH]^+/Z^-Pd(I)^+$ and $PdO/Pd(NO_3)_2$ sites were gradually converted to new Pd sites, which could adsorb NO_x and release at 218 °C. It could be observed that the peak at 218 °C shifted slightly to lower temperatures during the cycle tests, indicating that the newly generated Pd sites further changed. Furthermore, part of the Pd sites were converted to inactive Pd sites, resulting in a total decreased NO_x adsorption amount.

4.3. Sintering of Pd sites under high CO concentration

The adsorption amount of NO_x in each cycle, calculated via both NO_x adsorption and desorption branch, is shown in Fig. 3A. The correct material balance demonstrates all the adsorbed NO_x at 80 °C was released during TPD process in all cycles. The NO_x adsorption amount was significantly decreased in the first 7 cycles, resulting from the decreasing surface area of exposed Pd sites [8]. After the 7 cycles the deactivation leveled out and only a more moderate decrease in storage was observed. This degradation trend is similar to the sintering mode of supported metal active sites in catalysts, combined with Ostwald ripening and particle migration of metal cation sites, small clusters or nanoparticles [36]. We used a simple sintering law, $1/D^n = 1/D_0^n + kt$, to investigate the sintering mode, where D and D_0 are the Pd dispersion at time t and 0 (the time point for adding CO), respectively, and n is the exponent in the power law [37,38]. Since the dispersion of Pd is proportional to the Pd surface area and adsorbed NO_x amount, we here use the NO_x amount directly for the fitting. The value of n has been proposed to be 5 ~ 7 for particle migration [39] and ranging between 2 ~ 4 for Ostwald ripening [38]. In fitted result shown in Fig. 3B, the exponent n was fitted to 2 in the beginning of the cycles, but then changed to 6. Therefore, it could be deduced that Ostwald ripening contributed most to the Pd sintering in the beginning of test, while particle migration gradually became the dominant mechanism later in the test.

In our recent work [16], Pd/SSZ-13 synthesized in the same batch

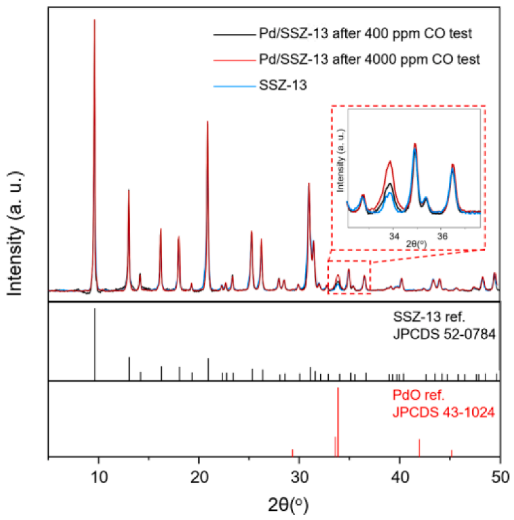

Fig. 4. XRD patterns of SSZ-13, Pd/SSZ-13 after 400 ppm CO/ 4000 ppm CO PNA test with reference patterns.

was previously evaluated in multicycle NO_x adsorption and TPD process, with 0–400 ppm NO_x, 0–400 ppm CO, 5% H_2O and 8% O_2. We found that the NO_x storage was enhanced under low CO concentration, while no PNA degradation has been found in multicycle test. To further investigate the PNA degradation under high CO concentration, the Pd/SSZ-13 samples after multicycle NO_x adsorption and TPD test were characterized by XRD and STEM-EDS to further confirm the CO induced sintering of Pd/SSZ-13. The sample after 400 ppm CO experiment was obtained from a PNA test with 2 cycles under 200 ppm CO and 2 cycles under 400 ppm CO, while the sample after 4000 ppm CO was obtained from a PNA experiment with 2 cycles without CO and 13 cycles under 4000 ppm CO. Fig. 4 shows the XRD patterns of Pd/SSZ-13 after a multicycle test. It could be seen that the main peaks of SSZ-13 in all samples are matched, showing that the structure of SSZ-13 was not changed after the multicycle test under different CO concentrations. However, the PdO(1 0 1) diffraction peak at $2\theta = 33.9°$ was increased after the multicycle test under 4000 ppm CO, demonstrating the agglomeration of PdO species. Note that also the pure SSZ-13 has a diffraction peak at the same position. The agglomeration of Pd was further confirmed by STEM-EDS as shown in Fig. 5, where the average diameter of Pd nanoparticles increased from 7.3 nm to 43.4 nm after the multicycle test under 4000 ppm CO (see Figure S2). The dispersion of Pd sites was measured via the CO irreversible adsorption (shown in Table 1), demonstrating that the Pd dispersion decreased from 44.0% to 9.1% after the multicycle test under 4000 ppm CO. Notably, the PdO (1 0 1) diffraction peak at $2\theta = 33.9°$ in the 400 ppm CO test is slightly larger than the one in SSZ-13, and we could also find a small number of large nano-particles (NPs) (83 nm) in this sample (Fig. 5A). This could be due to that some PdO particles are remaining from the incipient wetness impregnation during catalyst synthesis. The ion-exchanged Pd sites in Pd/SSZ-13 samples after 400/4000 ppm CO (including 200 ppm NO_x, 8% O_2 and 5% H_2O) PNA test were also determined by H_2-TPR, as shown in Figure S3. For the sample after 400 ppm PNA test, the H_2 consumption peak at ~ 155 °C is attributed to the reduction peak of ion-exchanged Pd (II) sites [40], and the H_2 consumption peak at ~ 518 °C could be attributed to the reduction peak of ion-exchanged Pd(I) because of the higher binding energy compared to Pd(II) sites [14]. The absence of these two H_2 consumption peaks in the sample after 4000 ppm PNA test indicates that almost all the ion-exchanged Pd sites agglomerated to large Pd NPs.

In-situ DRIFT was conducted to further investigate of Pd sintering mechanism during NO_x adsorption and TPD. These experiments were performed on scraped off wash-coat from monoliths either after degreening or multi-cycle experiments in the presence of 4000 ppm CO. It is widely reported that CO could be a probe molecule in in-situ DRIFT to detect the exposed Pd sites [23,41]. Accordingly, the DRIFT spectra of Pd/SSZ-13 samples were collected under 4000 ppm CO at 50 °C, as shown in Fig. 6A. The peaks were attributed to adsorbed CO on Pd species and –OH group, as marked in Fig. 6A. The relative peak intensity ratio between ν(CO-Pd) and ν(CO-OH) was calculated. It could be observed that ν(CO-Pd)/ν(CO-OH) decreased from 3.47 to 3.08 after multi-cycle experiments in the presence of 4000 ppm CO, consistent with the decreased amount of surface Pd species during the degradation. It is more obvious when we normalized the peak according to ν(CO-OH), as shown in the enlarged spectra on the upper left corner of Fig. 6A. All the ν(CO-Pd) peaks became weaker after multicycle tests, indicating the dispersion of Pd sites was decreased.

Table 1
Properties of Pd sites on Pd/SSZ-13 after multicycle NO_x adsorption and TPD test.

Sample	Pd crystalline size (nm)[a]	Pd dispersion (%)[b]
Pd/SSZ-13 after 400 ppm CO test	7.3	44.0
Pd/SSZ-13 after 4000 ppm CO test	43.4	9.1

[a] Average size measured from ~ 100 particles from STEM and TEM images
[b] Measured from CO irreversible adsorption

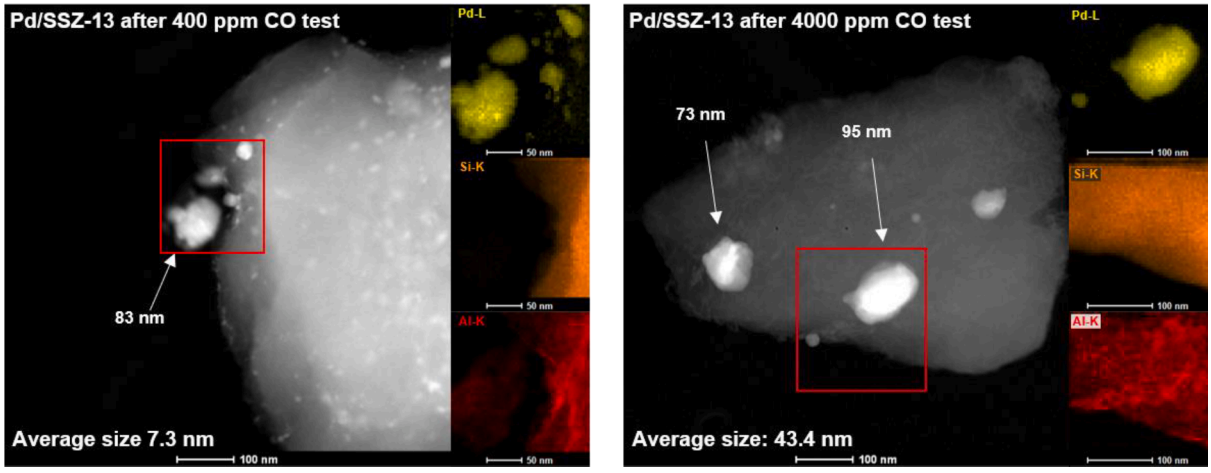

Fig. 5. STEM-EDS images of Pd/SSZ-13 samples after 400 ppm CO/ 4000 ppm CO (including 200 ppm NO_x, 8% O_2 and 5% H_2O) PNA test. The diameter statistics are shown in Figure S2.

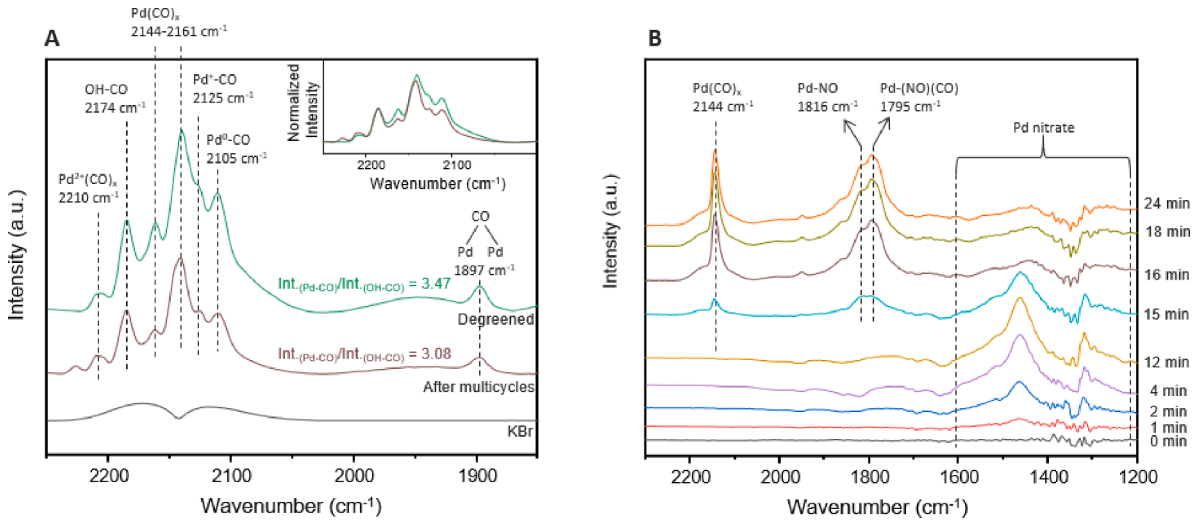

Fig. 6. (A) DRIFTS spectra of CO adsorption under 4000 ppm CO, at 50 °C on Pd/SSZ-13 samples after degreening and after multicycles with high CO concentration. (B) DRIFTS spectra under 200 ppm NO_x, 4000 ppm CO, 1% H_2O and 8% O_2 at 80 °C on degreened Pd/SSZ-13.

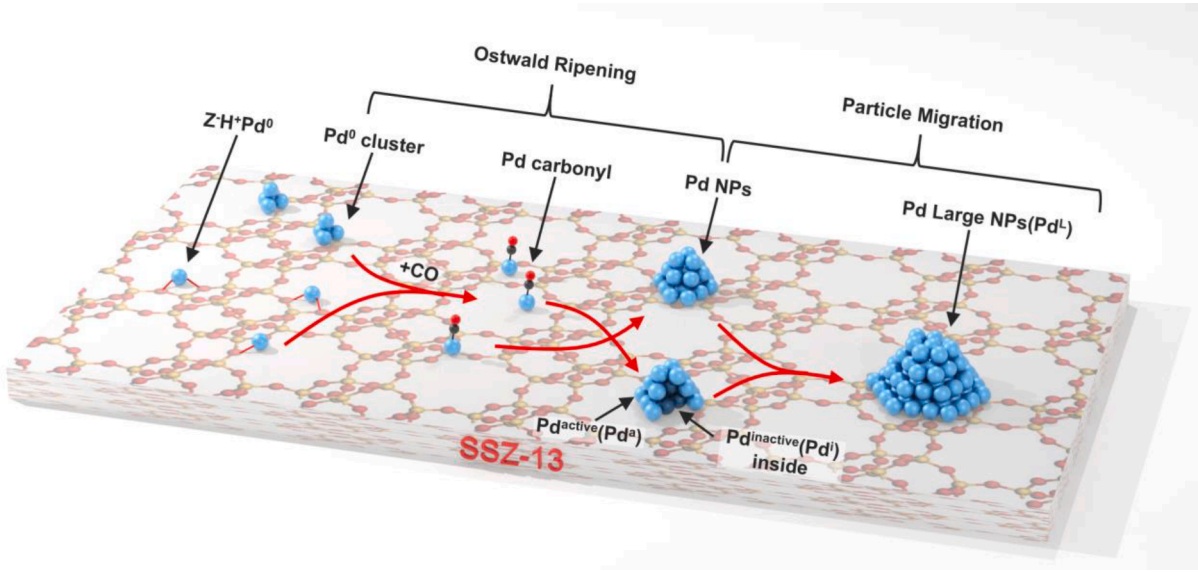

Fig. 7. Deactivation mechanism of Pd/SSZ-13 during PNA test under high CO concentration.

Owing to the significant change of PNA performance in the first cycle with CO, an in-situ DRIFT of CO and NO adsorption for the degreened sample was conducted to further investigate the degradation mode of PNA. The degreened Pd/SSZ-13 was first exposed to 200 ppm NO, 5% H_2O, 8%O_2 at 80 °C in the first 14 min, then 4000 ppm CO was added from 14 min. It could be seen the Pd nitrate species (1308 ~ 1700 cm^{-1}) [41] were generated when adding NO, then disappeared after adding CO. This result is due to the reduction of PdO species by CO occurs instead of forming $Pd(NO_3)_2$ [16]. After adding 4000 ppm CO, three peaks appeared at 2144 cm^{-1}, 1816 cm^{-1} and 1795 cm^{-1}, which are separately attributed to $Pd(CO)_x$, Pd-NO and Pd-(NO)(CO) species [42].

4.4. Degradation mechanism of Pd/SSZ-13

According to the experimental findings, a degradation mechanism of Pd/SSZ-13 is proposed, see Fig. 7. It could be found from DRIFT spectra (Fig. 6B) that $Pd(CO)_x$ species existed under high CO concentration (4000 ppm), while this species was not produced under low CO concentration (400 ppm) [16]. It is widely reported that CO could induce sintering by Ostwald ripening under high CO concentrations [36,43–45], where the formed $Pd(CO)_x$ species can diffuse easily on the bare support surface at room temperature [43,45]. With increased temperature, $Pd(CO)_x$ agglomerated and released CO to form larger Pd particles. Therefore, it is clear that Ostwald ripening of Pd species is one of the results of Pd/SSZ-13 degradation during multicycle NO_x adsorption and TPD in the presence of high CO levels (4000 ppm).

Furthermore, after the Pd species agglomerated via Ostwald ripening, the obtained Pd nano-particles (NPs) become less stable than the Pd cations and small Pd clusters form because of weak metal-support interactions [46,47]. Another sintering mode, particle migration, occurred when Pd NPs formed larger Pd NPs with a diameter of 43.4 nm (Fig. 5B). The sintering rate of particle migration is much lower than Ostwald ripening in the beginning of the evaluation when the dimension of Pd species is small [36]. However, the Ostwald ripening rate decreased drastically during the evaluation because the NPs are much more stable towards Ostwald ripening [48,49]. Subsequently, particle migration became the dominant mechanism for Pd sintering during the late of NO_x adsorption and TPD cycles. Therefore, it could be concluded

Table 2
Reaction mechanism for CO degradation of Pd/SSZ-13.

Reactions[a]	Reaction Steps[b]	Rate formations
R19	$Z^-Pd(II)Z^- + CO + H_2O \rightarrow Z^-H^+ + Z^-H^+$-Pd(0) + CO_2	$r_{19} = k_{19f}\Gamma_1\theta_{Sp1}y_{CO}y_{H2O}$
R20	$Z^-H^+ + Z^-H^+$-Pd(0) + $0.5O_2 \rightarrow Z^-Pd(II)Z^- + H_2O$	$r_{20} = k_{20f}(\Gamma_1\theta_{Sp12})y_{O2}^{0.5}$
R21	$Z^-H^+ + Z^-H^+$-Pd(0) + NO ⇌ $Z^-H^+ + Z^-H^+$-Pd(0)–NO	$r_{21} = k_{21f}\Gamma_1\theta_{Sp12}y_{NO} - k_{21b}\Gamma_1\theta_{Sp12\text{-}NO}$
R22	$Z^-H^+ + Z^-H^+$-Pd(0) + 4CO → $2Z^-H^+ + Pd(CO)_4$	$r_{22} = k_{22f}\Gamma_1\theta_{Sp12}y_{CO}^4$
R23	Z^-H^+-Pd(0) + 4CO → $Z^-H^+ + Pd(CO)_4$	$r_{23} = k_{23f}\Gamma_1\theta_{Sp23}y_{CO}^4$
R24	Pd(0) + 4CO → $Pd(CO)_4$	$r_{24} = k_{24f}\Gamma_3\theta_{Sp33}y_{CO}^4$
R25	$Pd(CO)_4$ ⇌ $Pd^{active(a)}$ + 4CO	$r_{25} = k_{25f}(\Gamma_1 + \Gamma_2 + \Gamma_3)\theta_{Sp41}y_{CO}^4$
R26	$Pd(CO)_4 \rightarrow Pd^{inactive(i)}$ + 4CO	$r_{26} = k_{26f}(\Gamma_1 + \Gamma_2 + \Gamma_3)\theta_{Sp41}y_{CO}^4$
R27	Pd^a + NO ⇌ Pd^a-NO	$r_{27} = k_{27f}(\Gamma_1 + \Gamma_2 + \Gamma_3)\theta_{Sp42}y_{NO} - k_{27b}(\Gamma_1 + \Gamma_2 + \Gamma_3)\theta_{Sp42\text{-}NO}$
R28	Pd^a-NO + O_2 ⇌ $Pd^aO + NO_2$	$r_{28} = k_{28f}(\Gamma_1 + \Gamma_2 + \Gamma_3)\theta_{Sp42\text{-}NO}y_{O2} - k_{28b}(\Gamma_1 + \Gamma_2 + \Gamma_3)\theta_{Sp43}y_{NO2}$
R29	Pd^a + $0.5O_2$ ⇌ Pd^aO	$r_{29} = k_{29f}(\Gamma_1 + \Gamma_2 + \Gamma_3)\theta_{Sp42}y_{O2}^{0.5} - k_{29b}(\Gamma_1 + \Gamma_2 + \Gamma_3)\theta_{Sp43}$
R30	Pd^aO + NO ⇌ $Pd^a + NO_2$	$r_{30} = k_{30f}(\Gamma_1 + \Gamma_2 + \Gamma_3)\theta_{Sp43}y_{NO} - k_{30b}(\Gamma_1 + \Gamma_2 + \Gamma_3)\theta_{Sp42}y_{NO2}$
R31	Pd^aO + CO → $Pd^a + CO_2$	$r_{31} = k_{31f}(\Gamma_1 + \Gamma_2 + \Gamma_3)\theta_{Sp43}y_{CO}$
R32	$Pd^a \rightarrow Pd^{Large\ NPs\ (L)}$	$r_{32} = k_{31f}(\Gamma_1 + \Gamma_2 + \Gamma_3)\theta_{Sp42}$
R33	Pd^L + NO ⇌ Pd^L-NO	$r_{33} = k_{33f}(\Gamma_1 + \Gamma_2 + \Gamma_3)\theta_{Sp44}y_{NO} - k_{33b}(\Gamma_1 + \Gamma_2 + \Gamma_3)\theta_{Sp44\text{-}NO}$
R34	Pd^L-NO + O_2 ⇌ $Pd^LO + NO_2$	$r_{34} = k_{34f}(\Gamma_1 + \Gamma_2 + \Gamma_3)\theta_{Sp44\text{-}NO}y_{O2} - k_{34b}(\Gamma_1 + \Gamma_2 + \Gamma_3)\theta_{Sp45}y_{NO2}$
R35	Pd^L + $0.5O_2$ ⇌ Pd^LO	$r_{35} = k_{35f}(\Gamma_1 + \Gamma_2 + \Gamma_3)\theta_{Sp44}y_{O2}^{0.5} - k_{35b}(\Gamma_1 + \Gamma_2 + \Gamma_3)\theta_{Sp45}$
R36	Pd^LO + NO ⇌ Pd^L + NO2	$r_{36} = k_{36f}(\Gamma_1 + \Gamma_2 + \Gamma_3)\theta_{Sp45}y_{NO} - k_{36b}(\Gamma_1 + \Gamma_2 + \Gamma_3)\theta_{Sp44}y_{NO2}$
R37	Pd^LO + CO → $Pd^L + CO_2$	$r_{37} = k_{37f}(\Gamma_1 + \Gamma_2 + \Gamma_3)\theta_{Sp45}y_{CO}$
Thermodynamic restrictions:		
Reactions	Overall reactions	Restrictions on parameters[c]
R27 + R28-R29	NO + $0.5O_2$ ⇌ NO_2	$\Delta H_{NOox} = [E_{f27}\text{-}E_{b27}(1\text{-}\alpha_{b27}\theta_{S42NO})] + (E_{f28}\text{-}E_{b28}) - (E_{f29}\text{-}E_{b29})$ $\Delta S_{NOox} = Rln(A_{f27}/A_{b27}) + Rln(A_{f28}/A_{b28}) - Rln(A_{f29}/A_{b29})$
R29 + R30	NO + $0.5O_2$ ⇌ NO_2	$\Delta H_{NOox} = (E_{f29}\text{-}E_{b29}) + (E_{f30}\text{-}E_{b30})$ $\Delta S_{NOox} = Rln(A_{f29}/A_{b29}) + Rln(A_{f30}/A_{b30})$
R33 + R34-R35	NO + $0.5O_2$ ⇌ NO_2	$\Delta H_{NOox} = [E_{f33}\text{-}E_{b33}(1\text{-}\alpha_{b33}\theta_{S44NO})] + (E_{f34}\text{-}E_{b34}) - (E_{f35}\text{-}E_{b35})$ $\Delta S_{NOox} = Rln(A_{f33}/A_{b33}) + Rln(A_{f34}/A_{b34}) - Rln(A_{f35}/A_{b35})$
R35 + R36	NO + $0.5O_2$ ⇌ NO_2	$\Delta H_{NOox} = (E_{f35}\text{-}E_{b35}) + (E_{f36}\text{-}E_{b36})$ $\Delta S_{NOox} = Rln(A_{f35}/A_{b35}) + Rln(A_{f36}/A_{b36})$

Storage sites:Γ_1:ZPd; Γ_2:ZPdOH; Γ_3:PdO
Storage species: Sp1: $Z^-Pd(II)Z^-$ Sp12: $Z^-H^+ + Z^-H^+$-Pd(0)
Sp21: $Z^-[Pd(II)OH]^+$ Sp22: $Z^-Pd(I)$ Sp23: Z^-H^+-Pd(0)
Sp31: Pd(II)O Sp32:$Pd(NO_3)_2$ Sp33: Pd(0)
Sp41: $Pd(CO)_4$ Sp42: Pd^a Sp43: Pd^aO Sp44: Pd^L Sp45: Pd^LO

[a] R1-18 was developed in our previous work [16] but also activated in current work. The reactions, rate expressions and thermodynamic restrictions are shown in Table S1.
[b] Corresponding parameters for R1-R37 are shown in Table S2.
[c] For the reactions with overall reaction of NO oxidation, the activation energy and pre-exceptional factors of all reactions need to meet the thermodynamic restriction, where ΔH_{NOox} = -58 kJ/mol and ΔS = -76 J/(K*mol).

that the Pd/SSZ-13 deactivated fast in the beginning and then became more slowly with increasing cycles, corresponding to the adsorbed NO_x amount shown in Fig. 3.

4.5. Kinetic model for CO induced degradation mechanism of Pd/SSZ-13

Based on the sintering mechanism of Pd as well as the previous reported kinetic model [16], an updated kinetic model with extra reactions R19-R37 was developed to describe the NO_x storage and release behavior as well as the Pd/SSZ-13 degradation during multiple cold start periods. The new reactions describing the deactivation are shown in Table 2. The thermodynamic restrictions can be found in Table 2 and all the corresponding parameters are shown in Table S2. R19-R21 were added to describe the changes in $Z^-Pd(II)Z^-$ under higher CO concentration. The $Z^-Pd(II)Z^-$ was reduced to Z^-H^+-Pd(0) and another empty Z^-H^+ sites by CO (R19) [14], and these two sites could be oxidized to $Z^-Pd(II)Z^-$ during the pretreatment step (R20). R21 accounts for the NO adsorption on Z^-H^+-Pd(0) site.

To describe the Ostwald ripening, the conversion of all the Pd(0) sites to Pd carbonyls [$Pd(CO)_4$] [43] was added in R22-R24. R25 and R26 describe the agglomeration and decomposition of $Pd(CO)_4$ species. We here define the Pd^{active} (Pd^a) as the exposed Pd sites on the surface of Pd NPs, while the $Pd^{inactive}$ (Pd^i) are enclosed within the Pd NPs, as shown in Fig. 7. Note that R25 is a reversible reaction because the surface Pd^a site could adsorb CO to form a carbonyl and agglomerate again via Ostwald ripening. The reactions on Pd NPs were added as R27-R31. R27 was firstly added to describe NO adsorption on Pd NPs. Moreover, both the metallic Pd site and oxidized PdO site contribute to NO oxidation [50], as described in R28 and R30. Furthermore, in the presence of O_2 and CO, R29 and R31 are added to account for the oxidation and reduction of Pd^a/PdO^a sites in Pd NPs. It should be noted that NO oxidation is the overall reaction for R27-R29 and R29-R30, where their parameters must fulfill thermodynamic restrictions shown in Table 2.

R32 was further added to explain the particle migration for the Pd NPs (Pd^a) sites to Pd large NPs (Pd^L). The particle migration of Pd^i sites is no longer considered because they are still inactive after further agglomeration. It is reported that the migration rate of Pd NPs is a thermally activated process: $\nu = \nu_0 e^{-Ea/kBT}$, where k_B is the Boltzmann constant, T the temperature, *Ea the* activation energy, and ν_0 is the attempt frequency for a move [51]. This rate formula is another form of the Arrhenius equation ($k = Ae^{-Ea/RT}$) in microscale version. Therefore, the Arrhenius equation is used as the rate expression for R32. The NO oxidation as well as the reduction and oxidation of Pd^L/PdO^L are described R33-R37 with thermodynamic restrictions, similar to the reactions on Pd^a/PdO^a (R27-R29). To simplify the model, the detachment of Pd atoms from large Pd nanoparticles (Pd^L) was not considered in our model, because the large Pd NPs are quite stable compared to small Pd NPs and ion-exchanged Pd sites.

4.6. Modeling results for multi-cycle NO_x adsorption under high CO concentration

According to the kinetic model (Table 2), the multi-cycle simulation and experimental results with 200 ppm NO_x, 4000 ppm CO (only in cycle 3–15), 8% O_2 and 5% H_2O were compared as shown in Fig. 8. It was found that the results in cycle 1 and cycle 2 are similar, and that the degradation therefore did start after adding 4000 ppm CO in cycle 3. The experimental results only slightly changed after cycle 7 because of the low sintering rate. Therefore, some of the results (cycle 1, 3–5, 7, 15) were selected and plotted versus time on stream, as shown in Fig. 9. The simulated result shows that the developed model can describe the main variation of changes in multi-cycle PNA test under high CO concentration. However, a small deviation in the end of every cycle (attributed to the overall NO oxidation) exists because the temperature measured by the thermocouple inside the monolith could not completely represent the temperature distribution over the whole monolith. Furthermore, although the NO_x binding energies and activation barrier of the reactions on one Pd site are set as constant in the kinetic model, they should also be influenced by the size of Pd sites, which is changing during the Pd sintering. Therefore, there are still slight deviations between the experiment and model, especially in the later cycles. The coverages of Pd species in cycle 1 predicted via kinetic model are shown in Figure S5. It could be seen that the peaks of NO desorption at 252 °C and 371 °C are attributed to the NO respectively releasing from $Z^-Pd(II)Z^-$ and $Z^-Pd(I)^+$, where NO reduced $Z^-[Pd(II)OH]^+$ to $Z^-Pd(I)^+$. The

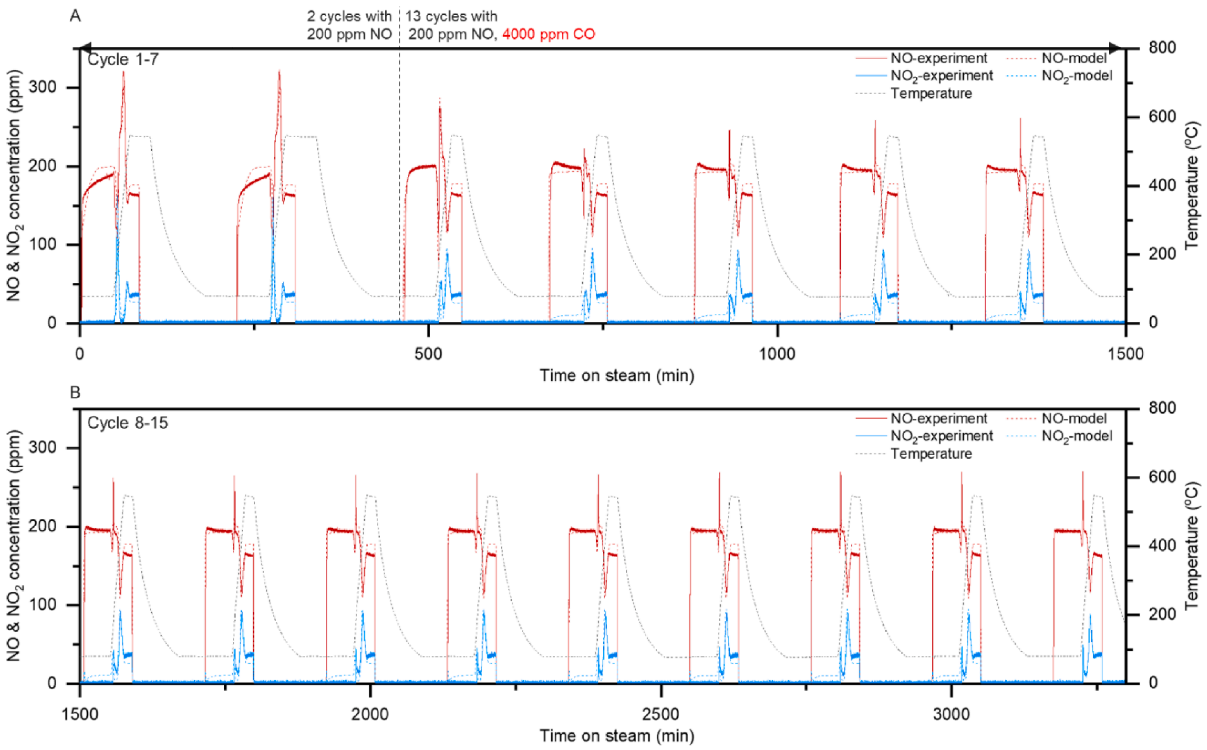

Fig. 8. NO_x profiles in experiment and model in multi-cycle test with high CO concentration. A: Cycle 1–7 (0 ~ 1500 min). B: Cycle 8–15 (1500 ~ 3100 min). Reaction conditions: 750 mL/min of total flow rate, 200 ppm NO_x (NO_2/NO_x = 1.8%), 4000 ppm CO (only in Cycle 3–15), 5% H_2O, 8% O_2, balanced in Ar. Detailed results of each cycle is also shown in Figure S4.

inverted peak of NO and NO_2 desorption peak at 166 °C are attributed to the reduction of $Z^-[Pd(II)OH]^+$ and $Pd(NO_3)_2$ decomposition respectively. Moreover, the coverages of initial $Z^-Pd(II)Z^-$, $Z^-[Pd(II)OH]^+$ and PdO sites were reached to 100% during the regeneration process, confirming that there is no deactivation on Pd/SSZ-13 before CO exposure. After cycle 3 the NO desorption peaks of $Z^-Pd(II)Z^-$–NO (252 °C) and $Z^-Pd(I)^+$–NO (371 °C) decreased and then disappeared quickly, while another peak appeared at 218 °C and then shifted to a lower temperature. The NO_2 desorption peak at 166 °C also decreased and shifted to lower temperature. These results indicate the sintering reaction induced by the addition of 4000 ppm CO addition, and agglomerated Pd sites were generated and contributed to NO_x adsorption instead of the three initial Pd sites.

Fig. 10A shows the coverage of total species in the different initial Pd sites. Part of the Pd species are converted to $Pd(CO)_4$ in the adsorption branch and are thereafter participating in the sintering reactions, as was observed in in-situ DRIFT where $Pd(CO)_4$ was formed. It could be seen that the initial ion-exchanged Pd sites ($Z^-Pd(II)Z^-$, $Z^-[Pd(II)OH]^+$) disappeared because of the degradation, which is also consistent with the H_2-TPR result (Figure S3), where no reduction peak of ion-exchanged Pd sites was found for the sample after the multi-cycle test. The initial Pd sites remain at 100% during the first 2 cycles, corresponding to the experimental and modeling results that there was no degradation occurring before adding high concentration of CO. After CO addition, these initial Pd sites gradually decreased in each cycle. It should be noted that a change of Pd sites differ in cycle 3 and cycle 4, while the trends of Pd coverage after cycle 5 are similar to cycle 4. Thus, the model predicted mean coverages in cycle 3 and cycle 4 are selected and shown in Fig. 10B, C to illustrate the degradation mechanism.

In the beginning of cycle 3 (see Fig. 10B), all the Pd species on the three initial Pd sites were decreased, and the total species in the Pd^a site ($Pd(CO)_4$, Pd^a-NO, Pd^a, Pd^aO) and Pd^i site were increased, where Pd^a is the notation for the active Pd sites on the surface of the Pd nano-particles (NPs), while the Pd^i represents the inactive Pd sites in the center of the particle (see Fig. 7). This increase of Pd^a and Pd^i demonstrates that the sintering started. During the NO_x adsorption at 80 °C, all the initial Pd species were reduced to Pd(0) species and subsequently CO was adsorbed to form $Pd(CO)_4$ species (R19-R24). Meanwhile, the $Pd(CO)_4$ agglomerated to NPs and partially formed inactive Pd (Pd^i) as depicted in Fig. 7 (R26). With the increased temperature, $Pd(CO)_4$ released CO and formed Pd^a and Pd^i species (R25-R26). It could also be seen that the Ostwald ripening rate increased. The generated surface Pd^a species started to adsorb NO and released at higher temperature, resulting in an NO release peak at ~ 218 °C (R27). Moreover, part of the NO species adsorbed on Pd^a (Pd^a-NO) were oxidized by O_2 (R28) instead of desorption, producing an NO_2 peak at ~ 210 °C. After desorption, the Pd^a sites were oxidized to Pd^aO sites by O_2 (R29) at ~ 280 °C, and Pd^aO sites were further reduced by NO and CO at higher temperature (R28-R29), resulting in an NO inverted peak and an NO_2 generation peak at the end of TPD procedure (~450 °C). Furthermore, the particle-migration sintering rate increased at this temperature, leading to the agglomeration of Pd^a NPs to large Pd nano-paricles (Pd^L) via R32, and then oxidized to Pd^LO (R35). It also found that around 5%~10% of Z^-H^+-Pd^0 sites and Pd^0 clusters among the initial Pd sites did not participate in the Ostwald ripening in cycle 3, and these species were re-oxidized back to initial $Z^-Pd(II)Z^-$, $Z^-[Pd(II)OH]^+$ and PdO sites in the regeneration procedure.

The model predicted coverages during cycle 4 are shown in Fig. 10C. It should be noted that the two sintering modes also occurred in cycle 4, where part of the initial Pd sites were converted to $Pd(CO)_4$ species and agglomerated to Pd nano-particles. Furthermore, the generated Pd NPs were sintered to larger Pd NPs via particle migration. In the beginning of cycle 4 at 80 °C, Pd^LO species were gradually reduced by CO and formed Pd^L species (R37). The reduction of Pd^LO sites is slow owing to the large size of NPs [52], and only the surface PdO species on Pd^LO sites could be reduced. Therefore, there was only around 10% of the Pd^LO sites reduced to Pd^L sites even at a higher temperature. The reduced Pd^L sites adsorbed NO via R33 and the coverage of Pd^L-NO reached only 7%,

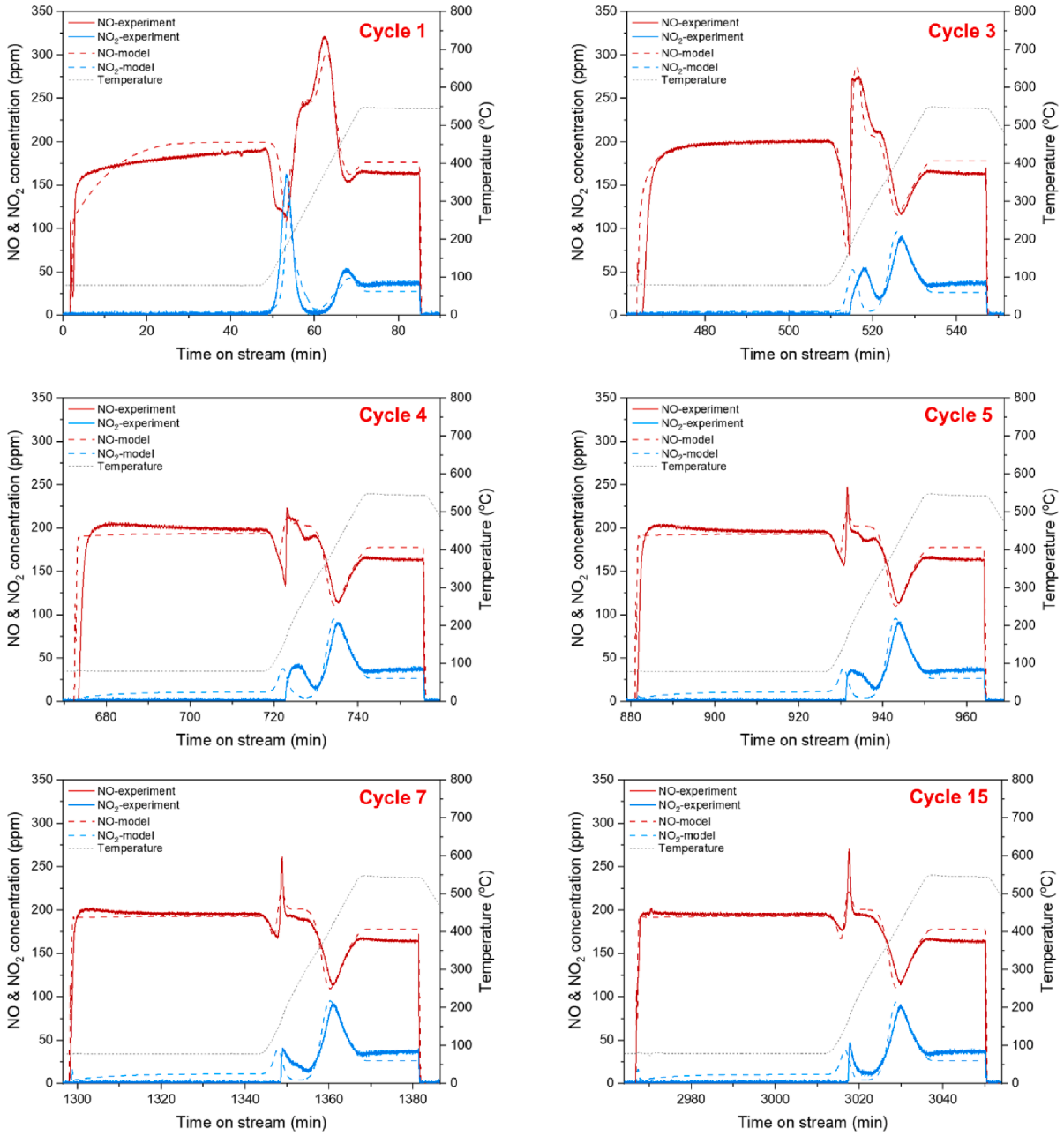

Fig. 9. Selected magnified experimental and modeling results of NO and NO_2 profile in Fig. 8. Reaction conditions: 750 mL/min of total flow rate, 200 ppm NO_x (NO_2/NO_x = 1.8%), 4000 ppm CO (only in Cycle 3–15), 5% H_2O, 8% O_2, balanced in Ar.

indicating the large Pd nanoparticle stores less NO_x species. Then, part of the Pd^L-NO species was decomposed and released NO at ~ 200 °C (R33), and the rest of them was oxidized by O_2 to produce NO_2 at ~ 180 °C (R36). R35 was also added to describe the oxidation of Pd^L to Pd^LO. The coverage in the regeneration part in cycle 4 is shown in Figure S6. Although there was a deactivation occurring during cycle 4, the distribution of the Pd sites was not significantly changed, resulting in similar NO_x adsorption behaviors between cycle 5 to 15. After the multi-cycle test, 65% of the total Pd sites are converted to the deactivated Pd sites (Pd^i), and part of the large Pd NPs did not participate in the NO_x adsorption because of the weak interaction. This is close to the change of the Pd dispersion obtained from the CO irreversible adsorption (79%, from Table 1).

We further validated the current kinetic model for NO_x adsorption and TPD under low CO concentration, as shown in Figure S7. The experimental results from Figure S7A and Figure S7B were respectively obtained under 200 ~ 400 ppm CO. Other gas conditions were the same as in the previous evaluation (Fig. 1), which includes 200 ppm NO_x, 5% H_2O and 8% O_2. It could be seen that the model could well predict the NO_x storage behavior, and the simulated results are similar to those without sintering reactions in our previous modeling work [16]. Furthermore, the model predicted coverages in Figure S7C, D demonstrate that the coverages of initial Pd sites returned to 100% in the regeneration procedure, indicating that there is no degradation under 200 ~ 400 ppm CO in the model, which agrees well with the experimental findings. Therefore, our model can be adequately applied for describing NO_x storages and release under different operating conditions with low CO concentration, while also suitably describing the high concentration CO induced degradation.

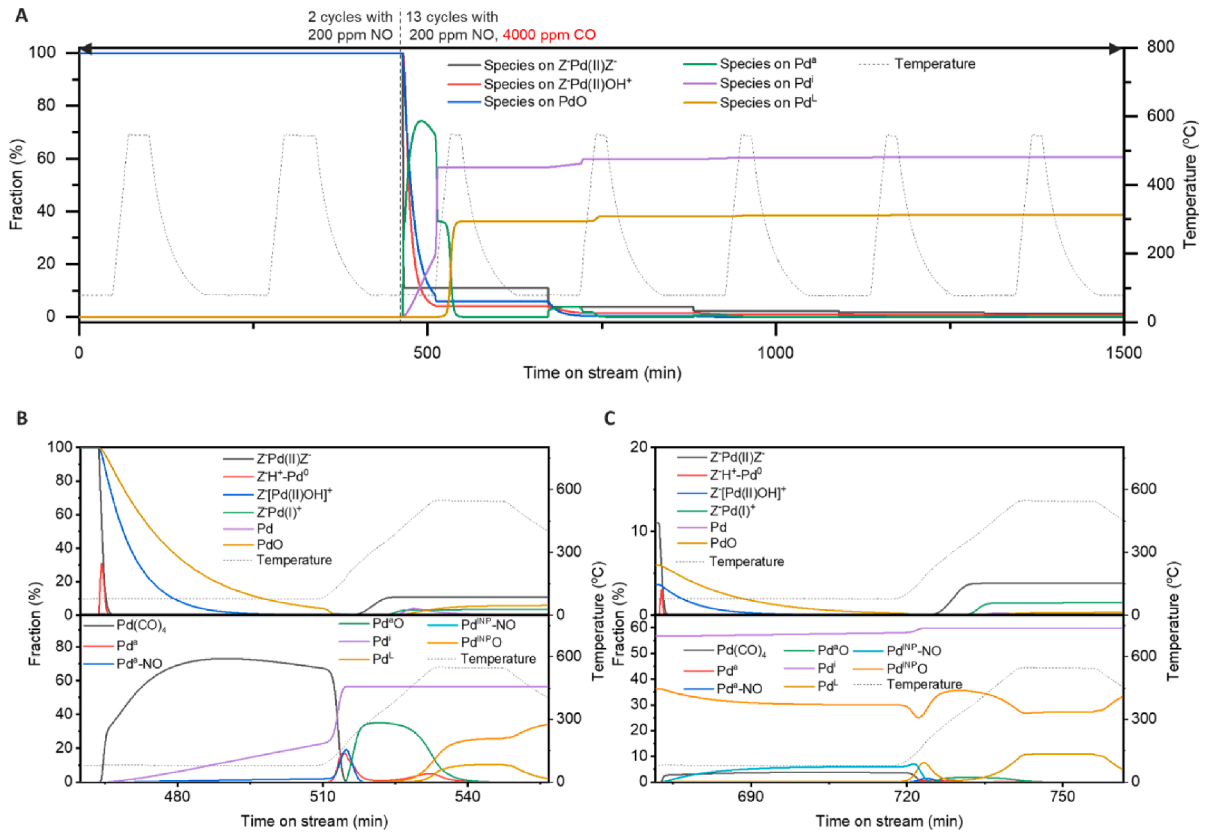

Fig. 10. Mean coverages of different species of PNA test with high CO concentration predicted via kinetic model. A: Coverage of total species in different initial Pd sites. B: Coverage of Pd species in cycle 3. C: Coverage of Pd species in cycle 4.

5. Conclusions

In summary, we have developed a kinetic model for describing the CO-induced PNA degradation. We first synthesized Pd/SSZ-13 and evaluated it as a PNA using NO_x adsorption and TPD process with multiple cycles, under varied component of inlet gases (200 ppm NO_x, 0–4000 ppm CO, 5%H_2O, 8%O_2 in Ar). According to the experimental behavior and the changes of Pd species during evaluation, we concluded that the Pd sintering mainly induces the PNA degradation. The sintering mode of Pd consists of Ostwald ripening and particle migration. In Ostwald ripening, the initial Pd sites, i.e. $Z^-Pd(II)Z^-$, $Z^-[Pd(II)OH]^+$ and PdO, were first reduced to metallic Pd sites, which then formed Pd carbonyl species under high CO concentration. Owing to the high mobility of Pd carbonyl species, they agglomerated to Pd nanoparticles with increased temperature. Pd NPs have weaker metal-support interaction, and consequently sintered via particle migration induced by high operating temperature, which is independent of the CO concentration. The sintering rate of Ostwald ripening is much higher than particle migration when the size of the Pd species was small, resulting in a fast degradation in the beginning of the multi-cycle test with 4000 ppm CO. When the size of the Pd species became larger, the sintering rate of Ostwald ripening decreased and particle migration became the dominant mechanism for deactivation. In addition, this model can well describe multi-cycle NO_x storage and release behavior under low CO concentration, where no degradation was observed in the experiment. In general, the model could be robustly applied for PNA in multiple cold start periods (200–400 ppm NO_x, 0–4000 ppm CO, 5%H_2O, 8%O_2 balanced in Ar), demonstrating a good prediction in both NO_x adsorption behavior and PNA degradation.

Declaration of Competing Interest

The authors declare that they have no known competing financial interests or personal relationships that could have appeared to influence the work reported in this paper.

Acknowledgment

This work was performed at the Division of Chemical Engineering and the Competence Center for Catalysis, Chalmers University of Technology, collaborated with AVL List GmbH. This project is funded from the European Union's Horizon 2020 research and innovation programme under grant agreement no 874972. We gratefully acknowledge Dr. Stefan Gustafsson and Dr. Ludvig de Knoop from CMAL (Chalmers material characterization laboratory) for their support with STEM.

Appendix A. Supplementary data

Supplementary data to this article can be found online at https://doi.org/10.1016/j.cej.2022.135714.

References

[1] A. Wang, L. Olsson, The impact of automotive catalysis on the United Nations sustainable development goals, Nat. Catal. 2 (7) (2019) 566–570, https://doi.org/10.1038/s41929-019-0318-3.
[2] C. Kim, G. Qi, K. Dahlberg, W. Li, Strontium-doped perovskites rival platinum catalysts for treating nox in simulated diesel exhaust, Science 327 (5973) (2010) 1624–1627, https://doi.org/10.1126/science.1184087.
[3] B. Kim, H. Jeong, J. Bae, P. Kim, C. Kim, H. Lee, Lean NOx trap catalysts with high low-temperature activity and hydrothermal stability, Appl. Catal. B-Environ. 270 (2020) 9, https://doi.org/10.1016/j.apcatb.2020.118871.
[4] A. Marberger, A. Petrov, P. Steiger, M. Elsener, O. Kröcher, M. Nachtegaal, D. Ferri, Time-resolved copper speciation during selective catalytic reduction of NO on Cu-

SSZ-13, Nat. Catal. 1 (3) (2018) 221–227, https://doi.org/10.1038/s41929-018-0032-6.
[5] C. Paolucci, I. Khurana, A. Parekh, S. Li, A.J. Shih, H. Li, J. Di Iorio, J. Albarracin-Caballero, A. Yezerets, J. Miller, W. Delgass, F. Ribeiro, W. Schneider, R. Gounder, Dynamic multinuclear sites formed by mobilized copper ions in NOx selective catalytic reduction, Science 357 (6354) (2017) 898–903, https://doi.org/10.1126/science.aan5630.
[6] J. Lee, J. Theis, E. Kyriakidou, Vehicle emissions trapping materials: Successes, challenges, and the path forward, Appl. Catal. B-Environ. 243 (2019) 397–414, https://doi.org/10.1016/j.apcatb.2018.10.069.
[7] K. Khivantsev, N.R. Jaegers, L. Kovarik, J.C. Hanson, F. Tao, Y.U. Tang, X. Zhang, I. Z. Koleva, H.A. Aleksandrov, G.N. Vayssilov, Y. Wang, F. Gao, J. Szanyi, Achieving atomic dispersion of highly loaded transition metals in small-pore zeolite SSZ-13: High-capacity and high-efficiency low-temperature CO and passive NOx adsorbers, Angew. Chem. Int. Ed. 57 (51) (2018) 16672–16677, https://doi.org/10.1002/anie.201809343.
[8] Y. Gu, R.P. Zelinsky, Y.-R. Chen, W.S. Epling, Investigation of an irreversible NOx storage degradation Mode on a Pd/BEA passive NOx adsorber, Appl. Catal. B-Environ. 258 (2019) 118032, https://doi.org/10.1016/j.apcatb.2019.118032.
[9] Y. Ryou, J. Lee, S. Cho, H. Lee, C. Kim, D. Kim, Activation of Pd/SSZ-13 catalyst by hydrothermal aging treatment in passive NO adsorption performance at low temperature for cold start application, Appl. Catal. B-Environ. 212 (2017) 140–149, https://doi.org/10.1016/j.apcatb.2017.04.077.
[10] M. Ambast, K. Karinshak, B.M.M. Rahman, L.C. Grabow, M.P. Harold, Passive NOx adsorption on Pd/H-ZSM-5: Experiments and modeling, Appl. Catal. B-Environ. 269 (2020) 118802, https://doi.org/10.1016/j.apcatb.2020.118802.
[11] Y. Zheng, L. Kovarik, M.H. Engelhard, Y. Wang, Y. Wang, F. Gao, J. Szanyi, Low-temperature Pd/zeolite passive NOx adsorbers: structure, performance, and adsorption chemistry, J. Phys. Chem. C 121 (29) (2017) 15793–15803, https://doi.org/10.1021/acs.jpcc.7b0431210.1021/acs.jpcc.7b04312.s001.
[12] K. Mandal, Y. Gu, K.S. Westendorff, S. Li, J.A. Pihl, L.C. Grabow, W.S. Epling, C. Paolucci, Condition-dependent Pd speciation and NO adsorption in Pd/zeolites, ACS Catal. 10 (21) (2020) 12801–12818, https://doi.org/10.1021/acscatal.0c0358510.1021/acscatal.0c03585.s00110.1021/acscatal.0c03585.s002.
[13] A. Gupta, S. Kang, M. Harold, NOx uptake and release on Pd/SSZ-13: Impact Of Feed composition and temperature, Catal. Today 360 (2021) 411–425, https://doi.org/10.1016/j.cattod.2020.01.018.
[14] D. Mei, F. Gao, J. Szanyi, Y. Wang, Mechanistic insight into the passive NOx adsorption in the highly dispersed Pd/HBEA zeolite, Appl. Catal. A-Gen. 569 (2019) 181–189, https://doi.org/10.1016/j.apcata.2018.10.037.
[15] M. Ambast, A. Gupta, B.M.M. Rahman, L.C. Grabow, M.P. Harold, NOx adsorption with CO and C_2H_4 on Pd/SSZ-13: Experiments and modeling, Appl. Catal. B-Environ. 286 (2021) 119871, https://doi.org/10.1016/j.apcatb.2020.119871.
[16] D. Yao, R. Feizie Ilmasani, J.C. Wurzenberger, T. Glatz, J. Han, A. Wang, D. Creaser, L. Olsson, Kinetic modeling of CO assisted passive NOx adsorption on Pd/SSZ-13, Chem. Eng. J. 428 (2022) 132459, https://doi.org/10.1016/j.cej.2021.132459.
[17] L. Fang, D. Lou, Z. Hu, P. Tan, The emission characteristics of a diesel engine during start-up process at different altitudes, Energies. 12 (2021) 3556–3571, https://doi.org/10.3390/en12183556.
[18] Y. Gu, S. Marino, M. Cortés-Reyes, I.S. Pieta, J.A. Pihl, W.S. Epling, Integration of an Oxidation Catalyst with Pd/Zeolite-Based Passive NOx Adsorbers: Impacts on Degradation Resistance and Desorption Characteristics, Ind. Eng. Chem. Res. 60 (18) (2021) 6455–6464, https://doi.org/10.1021/acs.iecr.0c0518610.1021/acs.iecr.0c05186.s001.
[19] J. Theis, J. Ura, Assessment of zeolite-based Low temperature NOx adsorbers: Effect of reductants during multiple sequential cold starts, Catal. Today 360 (2021) 340–349, https://doi.org/10.1016/j.cattod.2020.01.040.
[20] A. Wang, K. Xie, A. Kumar, K. Kamasamudram, L. Olsson, Layered Pd/SSZ-13 with Cu/SSZ-13 as PNA − SCR dual-layer monolith catalyst for NOx abatement, Catal. Today 360 (2021) 356–366, https://doi.org/10.1016/j.cattod.2020.01.035.
[21] F. Gao, N. Washton, Y. Wang, M. Kollár, J. Szanyi, C. Peden, Effects of Si/Al ratio on Cu/SSZ-13 NH3-SCR catalysts: Implications for the active Cu species and the roles of Brønsted acidity, J. Catal. 331 (2015) 25–38, https://doi.org/10.1016/j.jcat.2015.08.004.
[22] K. Wijayanti, S. Andonova, A. Kumar, J. Li, K. Kamasamudram, N. Currier, A. Yezerets, L. Olsson, Impact of sulfur oxide on NH3-SCR over Cu-SAPO-34, Appl. Catal. B-Environ. 166–167 (2015) 568–579, https://doi.org/10.1016/j.apcatb.2014.11.043.
[23] S. Yasumura, H. Ide, T. Ueda, Y. Jing, C. Liu, K. Kon, T. Toyao, Z. Maeno, K.-I. Shimizu, Transformation of Bulk Pd to Pd Cations in Small-Pore CHA Zeolites Facilitated by NO, JACS Au 1 (2) (2021) 201–211, https://doi.org/10.1021/jacsau.0c0011210.1021/jacsau.0c00112.s00110.1021/jacsau.0c00112.s002.
[24] A.L. GmbH, AVL BOOST Aftertreatment Manual, (2020).
[25] D. Chatterjee, T. Burkhardt, B. Bandl-Konrad, T. Braun, E. Tronconi, I. Nova, C. Ciardelli, Numerical simulation of ammonia SCR-catalytic converters: Model development and application, SAE Transactions 114 (2005) 437–448.
[26] S. Tamm, L. Olsson, S. Fogel, P. Gabrielsson, M. Skoglundh, A kinetic model of the hydrogen assisted selective catalytic reduction of NO with ammonia over Ag/Al_2O_3, AIChE J. 59 (11) (2013) 4325–4333, https://doi.org/10.1002/aic.14170.
[27] L. Olsson, K. Wijayanti, K. Leistner, A. Kumar, S.Y. Joshi, K. Kamasamudram, N. W. Currier, A. Yezerets, A multi-site kinetic model for NH3-SCR over Cu/SSZ-13, Appl. Catal. B-Environ. 174–175 (2015) 212–224, https://doi.org/10.1016/j.apcatb.2015.02.037.
[28] L. Olsson, H. Sjövall, R. Blint, A kinetic model for ammonia selective catalytic reduction over Cu-ZSM-5, Appl. Catal. B-Environ. 81 (3–4) (2008) 203–217, https://doi.org/10.1016/j.apcatb.2007.12.011.
[29] Supriyanto, K. Wijayanti, A. Kumar, S. Joshi, K. Kamasamudram, N.W. Currier, A. Yezerets, L. Olsson, Global kinetic modeling of hydrothermal aging of NH3-SCR over Cu-zeolites, Appl. Catal. B-Environ. 163 (2015) 382–392, https://doi.org/10.1016/j.apcatb.2014.07.059.
[30] L. Olsson, K. Wijayanti, K. Leistner, A. Kumar, S. Joshi, K. Kamasamudram, N. Currier, A. Yezerets, A kinetic model for sulfur poisoning and regeneration of Cu/SSZ-13 used for NH_3-SCR, Appl. Catal. B-Environ. 183 (2016) 394–406, https://doi.org/10.1016/j.apcatb.2015.11.001.
[31] A. Wang, P. Arora, D. Bernin, A. Kumar, K. Kamasamudram, L. Olsson, Investigation of the robust hydrothermal stability of Cu/LTA for NH3-SCR reaction, Appl. Catal. B-Environ. 246 (2019) 242–253, https://doi.org/10.1016/j.apcatb.2019.01.039.
[32] L. Olsson, M. Fredriksson, R. Blint, Kinetic modeling of sulfur poisoning and regeneration of lean NOx traps, Appl. Catal. B-Environ. 100 (1–2) (2010) 31–41, https://doi.org/10.1016/j.apcatb.2010.07.004.
[33] X. Auvray, W. Partridge, J. Choi, J. Pihl, F. Coehlo, A. Yezerets, K. Kamasamudram, N. Currier, L. Olsson, Kinetic modeling of NH_3-SCR over a supported Cu zeolite catalyst using axial species distribution measurements, Appl. Catal. B-Environ. 163 (2015) 393–403, https://doi.org/10.1016/j.apcatb.2014.08.003.
[34] L. Olsson, H. Sjövall, R. Blint, Detailed kinetic modeling of NOx adsorption and NO oxidation over Cu-ZSM-5, Appl. Catal. B-Environ. 87 (3) (2009) 200–210, https://doi.org/10.1016/j.apcatb.2008.09.007.
[35] J. Xu, M. Harold, V. Balakotaiah, Modeling the effects of Pt loading on NOx storage on Pt/BaO/Al2O3 catalysts, Appl. Catal. B-Environ. 104 (3–4) (2011) 305–315, https://doi.org/10.1016/j.apcatb.2011.03.014.
[36] T. Hansen, A. DeLaRiva, S. Challa, A. Datye, Sintering of catalytic nanoparticles: particle migration or ostwald ripening? Acc. Chem. Res. 46 (8) (2013) 1720–1730, https://doi.org/10.1021/ar3002427.
[37] Q. Xu, K. Kharas, B. Croley, A. Datye, The Sintering of Supported Pd Automotive Catalysts, ChemCatChem 3 (6) (2011) 1004–1014, https://doi.org/10.1002/cctc.201000392.
[38] P. Wynblatt, N. Gjostein, Particle growth in model supported metal catalysts—I, Theory, Acta Metallurgica 24 (12) (1976) 1165–1174, https://doi.org/10.1016/0001-6160(76)90034-1.
[39] P. Harris, Growth and structure of supported metal catalyst particles, Inter. Mater. Rev. 40 (3) (1995) 97–115, https://doi.org/10.1179/imr.1995.40.3.97.
[40] Y. Ryou, J. Lee, Y. Kim, S. Hwang, H. Lee, C.H. Kim, D.H. Kim, Effect of reduction treatments (H_2 vs. CO) on the NO adsorption ability and the physicochemical properties of Pd/SSZ-13 passive NO_x adsorber for cold start application, Appl. Catal. A: Gen. 569 (2019) 28–34, https://doi.org/10.1016/j.apcata.2018.10.016.
[41] K. Khivantsev, N.R. Jaegers, I.Z. Koleva, H.A. Aleksandrov, L. Kovarik, M. Engelhard, F. Gao, Y. Wang, G.N. Vayssilov, J. Szanyi, Stabilization of super electrophilic Pd^{+2} cations in small-pore SSZ-13 zeolite, J Phys. Chem. C 124 (1) (2020) 309–321, https://doi.org/10.1021/acs.jpcc.9b0676010.1021/acs.jpcc.9b06760.s001.
[42] T. Baidya, P. Bera, B.D. Mukri, S.K. Parida, O. Kröcher, M. Elsener, M.S. Hegde, DRIFTS studies on CO and NO adsorption and NO+CO reaction over Pd^{2+}-substituted CeO2 and $Ce_{0.75}Sn_{0.25}O_2$ catalysts, J. Catal. 303 (2013) 117–129, https://doi.org/10.1016/j.jcat.2013.03.020.
[43] J. Li, G. Schreckenbach, T. Ziegler, A Reassessment of the first metal-carbonyl dissociation energy in M(CO)4 (M = Ni, Pd, Pt), M(CO)5 (M = Fe, Ru, Os), and M(CO)6 (M = Cr, Mo, W) by a quasirelativistic density functional method, J. Am. Chem. Soc. 117 (1) (1995) 486–494, https://doi.org/10.1021/ja00106a056.
[44] R. Ouyang, J. Liu, W. Li, Atomistic theory of ostwald ripening and disintegration of supported metal particles under reaction conditions, J. Am. Chem. Soc. 135 (5) (2013) 1760–1771, https://doi.org/10.1021/ja3087054.
[45] G. Parkinson, Z. Novotny, G. Argentero, M. Schmid, J. Pavelec, R. Kosak, P. Blaha, U. Diebold, Carbon monoxide-induced adatom sintering in a Pd-Fe3O4 model catalyst, Nat. Mater. 12 (8) (2013) 724–728, https://doi.org/10.1038/nmat3667.
[46] C. Campbell, S. Parker, D. Starr, The effect of size-dependent nanoparticle energetics on catalyst sintering, Science 298 (5594) (2002) 811–814, https://doi.org/10.1126/science.1075094.
[47] J. Farmer, C. Campbell, Ceria maintains smaller metal catalyst particles by strong metal-support bonding, Science 329 (5994) (2010) 933–936, https://doi.org/10.1126/science.1191778.
[48] L. Liu, M. Lopez-Haro, C. Lopes, C. Li, P. Concepcion, L. Simonelli, J. Calvino, A. Corma, Regioselective generation and reactivity control of subnanometric platinum clusters in zeolites for high-temperature catalysis, Nat. Mater. 18 (8) (2019) 866–873, https://doi.org/10.1038/s41563-019-0412-6.
[49] S. Challa, A. Delariva, T. Hansen, S. Helveg, J. Sehested, P. Hansen, F. Garzon, A. Datye, Relating rates of catalyst sintering to the disappearance of individual nanoparticles during ostwald ripening, J. Am. Chem. Soc. 133 (51) (2011) 20672–20675, https://doi.org/10.1021/ja208324n.

[50] X. Auvray, L. Olsson, Stability and activity of Pd-, Pt- and Pd–Pt catalysts supported on alumina for NO oxidation, Appl. Catal. B-Environ. 168–169 (2015) 342–352, https://doi.org/10.1016/j.apcatb.2014.12.035.
[51] T. Gerber, J. Knudsen, P.J. Feibelman, E. Grånäs, P. Stratmann, K. Schulte, J. N. Andersen, T. Michely, CO-induced smoluchowski ripening of pt cluster arrays on the graphene/Ir(111) Moiré, ACS Nano 7 (3) (2013) 2020–2031, https://doi.org/10.1021/nn400082w.
[52] B. Zhu, G. Thrimurthulu, L. Delannoy, C. Louis, C. Mottet, J. Creuze, B. Legrand, H. Guesmi, Evidence of Pd segregation and stabilization at edges of AuPd nanoclusters in the presence of CO: A combined DFT and DRIFTS study, J. Catal. 308 (2013) 272–281, https://doi.org/10.1016/j.jcat.2013.08.022.